MAGNETISM

Atomic-scale visualization of topological spin textures in the chiral magnet MnGe

Jacob Repicky[1], Po-Kuan Wu[1], Tao Liu[1,2], Joseph P. Corbett[1], Tiancong Zhu[1], Shuyu Cheng[1], Adam S. Ahmed[1], N. Takeuchi[3], J. Guerrero-Sanchez[3], Mohit Randeria[1], Roland K. Kawakami[1], Jay A. Gupta[1]*

Topological spin textures in chiral magnets such as manganese germanide (MnGe) are of fundamental interest and may enable magnetic storage and computing technologies. Our spin-polarized scanning tunneling microscopy images of MnGe thin films reveal a variety of textures that are correlated to the atomic-scale structure. Our images indicate helical stripe domains, in contrast to bulk, and associated helimagnetic domain walls. In combination with micromagnetic modeling, we can deduce the three-dimensional (3D) orientation of the helical wave vectors, and we find that three helical domains can meet in two distinct ways to produce either a "target-like" or a "π-like" topological spin texture. The target-like texture can be reversibly manipulated through either current/voltage pulsing or applied magnetic field, which represents a promising step toward future applications.

Topological spin textures in chiral magnets are of interest both to fundamental science, through Berry phase–induced Hall effects, and for potential device applications, including magnetic racetrack memories and neuromorphic computing (*1*–*8*). Competing magnetic interactions lead to spin textures such as helices, where spins periodically tumble with a characteristic pitch length, and magnetic skyrmions, which are whirling localized textures with a total π rotation of the spins. In many cases of interest, the competition is between ferromagnetic exchange, which favors aligned spins, and the Dzyaloshinskii-Moriya interaction (DMI), which favors perpendicular spins and arises from spin-orbit coupling in the presence of broken inversion symmetry (*9*). The noncentrosymmetric "B20" crystal structure breaks bulk inversion symmetry, and magnetic skyrmions were first discovered in B20 MnSi (*9*) and FeGe (*10*). In these materials, the magnetic phase diagram and its evolution from bulk crystals to thin films are now well understood. Within the B20 family, MnGe is an intriguing outlier (*11*), with a helical pitch length of 2.8 nm that is more than an order of magnitude smaller than in other B20 crystals (*12*) and whose bulk phase diagram shows unusual "hedgehog-antihedgehog" crystals, for reasons that are not well understood (*13*–*15*). Spin-polarized scanning tunneling microscopy (SP-STM) is uniquely suited to probe the rich physics of such nanoscale spin textures in real space and provides microscopic insights that complement those obtained from ensemble techniques that may average over different chiral domains (*16*).

[1]Department of Physics, The Ohio State University, Columbus, OH 43210, USA. [2]University of Electronic Science and Technology of China, Chengdu 610054, China. [3]Centro de Nanociencias y Nanotecnologia, Universidad Nacional Autónoma de México, Apartado Postal 14, Ensenada Baja California, Código Postal 22800, Mexico.
*Corresponding author. Email: gupta.208@osu.edu

We used SP-STM to probe the magnetism on the surface of 80-nm-thick MnGe(111) films with atomic resolution. Our SP-STM images revealed a variety of topological spin textures depending on the local nanoscale structure, which we interpreted using micromagnetic modeling that builds on recent advances in the theory of helimagnetic domain walls (*17*). Figure 1, A and B, shows atomically resolved topographic images of the MnGe(111) surface. These images are consistent with the B20 structure of MnGe, which features alternating Mn and Ge layers with atoms arranged in triangular lattices of single atoms or trimers (*18*). The structure comprises a quadruple layer of alternating planes of Mn and Ge atoms with sparse or dense packing; the atomic arrangements exactly repeat after a sequence of three such layers. The relative stacking order and orientation of these layers determine the structural and magnetic chiralities (*19*–*22*). The surface lattice constant from these images is 0.67 ± 0.01 nm, within experimental uncertainty of the expected bulk value for the (111) surface (0.678 nm). Point defects on the surface are imaged with bright and dark contrast, but they do not affect the magnetic textures reported here.

In addition to the topographic information, Fig. 1, A and B, shows a subtle (~5 pm) periodic modulation of the atomic corrugation, reflecting the surface magnetic texture picked up by the SP-STM tip. This modulation is evident in the topographic linecut shown in Fig. 1C. To better isolate the stripe pattern from the topography in Fig. 1A, we performed a fast Fourier transform (FFT) (Fig. 1D). In addition to the primary hexagonal spot pattern from the MnGe atomic lattice, there are satellite spots corresponding to scattering vectors of $\pm\mathbf{q}$, rotated by $\phi \sim 14°$ with respect to the lattice. An inverse FFT image of the area, computed with only the atomic lattice and satellite spots, clearly resolves the stripe pattern while removing obscuration from the point defects (Fig. 1E). In bulk MnGe crystals, a 3D hedgehog lattice was observed with Lorentz transmission electron microscopy (LTEM) (*12*), which would yield a 2D lattice projected onto the surface, in contrast to the observed stripe pattern here (*18*). Furthermore, from the FFT analysis we measure a stripe period of 5.96 nm, which is considerably larger than the helical pitch length for bulk MnGe (2.8 nm).

This stripe pattern is consistent with a $1\mathbf{Q}$ helical state in these MnGe thin films, in contrast to the $3\mathbf{Q}$ state observed in bulk crystals. A priori, one could explain the stripe contrast with helices anchored to the surface plane as reported for FeGe (*17*), but this is contradicted by the larger observed pitch length. Prior neutron scattering studies in MnGe thin films indicate that the magnitude of $Q = 2.2\ \mathrm{nm}^{-1}$ is unchanged from the bulk value (*23*), and we expect that any additional surface-specific effects, such as reduced exchange or enhanced surface DMI, would lead to an even smaller pitch length, in contrast to the observation. Instead, we consider the tilting of $\mathbf{Q}$ toward the film normal [111] direction by a polar angle θ, which was invoked in the neutron studies (*23*). Following conventions for topological defects in chiral magnets (*24*, *25*), states with wave vectors $\mathbf{Q}$ and $-\mathbf{Q}$ correspond to the same helical structure, and we chose a positive projection along the surface normal $\hat{z} = (111)$. We defined the surface wave vector $\mathbf{q}$ as the projection of $\mathbf{Q}$ in the plane of the surface (i.e., $q = Q \sin\theta$), so that the polar tilt angle can be related to the observed real-space periodicity by $\theta = \sin^{-1}[2\pi/(Q \cdot 5.96\ \mathrm{nm})] = 28.6°$, compared to the bulk angle of 54.7° with $\mathbf{Q}$s along (100). Our estimated q is roughly consistent with the neutron studies, where a linearly decreasing tilt angle with decreasing film thickness down to 160 nm was attributed to strain-dependent magnetic anisotropy (*23*).

To directly probe the sensitivity of the spin helices to strain in real space, we imaged regions of the film where small curvatures are indicative of inhomogeneous strain. For example, in a different microscopic region of the sample shown in Fig. 2A, three terraces were observed, separated in height by steps of one quadruple layer each in the layered MnGe structure. Focusing on the middle terrace, topography line profiles show small (<0.1%) but significant bowing and curvature of the surface along the horizontal direction (Fig. 2B, blue profile). We note that these images are atomically resolved and the lattice spacing does not show any significant variation, but our experimental uncertainty in this measurement (~0.5%) is larger than the 0.1% height variation shown in the image.

To examine the stripe patterns over larger distances in such areas, we simultaneously mapped the differential conductance signal,

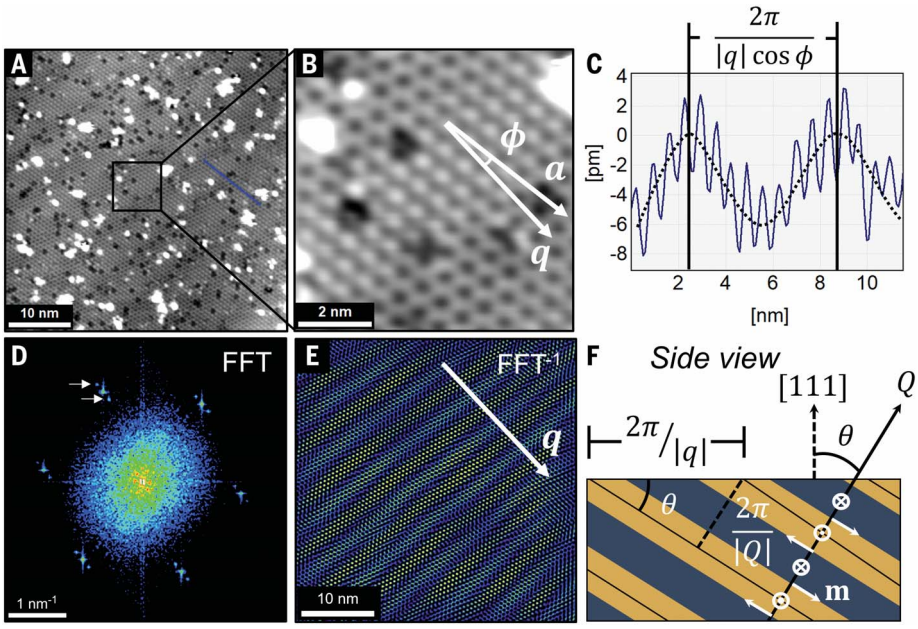

Fig. 1. Atomic-resolution SP-STM imaging of spin helices in MnGe. (**A**) Topographic image of the MnGe(111) surface (−0.17 V, 0.54 nA, T = 5 K). The helical magnetic texture is imaged as modulation in the atomic corrugation. (**B**) Close-up view of the outlined area in (A). Bright and dark lattice spots are observed, depending on the relative alignment between tip and surface spins. In this area, the surface projection of the helical wave vector **q** is rotated from the atomic lattice vector by an angle $\phi \approx 14°$. (**C**) Line profile taken at the blue line in (A) along nearest-neighbor atoms on the surface, showing the helical periodicity of 5.96 nm. The dotted line is a guide to the eye. (**D**) FFT image of the area in (A). Arrows indicate satellite peaks due to the surface-projected **q**. (**E**) Inverse FFT image produced by passing only the atomic lattice and satellite peaks in (D), allowing an unobstructed view of the stripe pattern and its effect on the atomic corrugation. (**F**) Schematic side view of the 3D helical texture showing the relation among **Q**, **q**, and the real-space modulations.

which relates to the spin-dependent density of states. Our SP-STM simulations (fig. S17) explore the expected magnetic contrast for textures with varying **Q** and tip magnetization vector $\mathbf{m}_{tip}$. Because the textures here represent a helical whirling of spins with both in-plane and out-of-plane components, magnetic contrast occurs for any combination of **Q** and $\mathbf{m}_{tip}$, except for the special case $\mathbf{m}_{tip} \parallel \mathbf{Q}$ where there is zero contrast. Figure 2C shows an SP-STM map of the area, where faint magnetic contrast reveals stripes along different directions and more complicated patterns. During repeated imaging of this area, we observed a complete reversal in magnetic contrast associated with an inversion of the tip's spin polarization (Fig. 2D). To confirm these stripes as magnetic in origin, we computed a difference image in Fig. 2E, as topographic or electronic contributions to the STM image would not invert under otherwise identical tunneling conditions. Whereas the magnetic contrast is absent in the sum image (fig. S16), the difference image accentuates intersections, bowing, and terminations of the stripe patterns in this area. We attribute these spin textures to local variations in the orientation of **Q**. For example, the observed stripe periodicity in Fig. 2E varies in the range of 6 to 10 nm depending on position, corresponding to respective variations $28° > \theta > 17°$ in the polar angle of **Q**. The stripe curvature and intersection points furthermore indicate helical domains with distinct azimuthal angles of **Q**.

To understand these features, we used a phenomenological model that builds on recent advances in the theory of topological domain walls in helimagnets (*17*) and uses inputs from neutron data (*23*) to constrain the magnetic anisotropy and hence the orientations of the helical wave vectors (*18*). The structure of a domain wall between two helical regions depends primarily on the angle θ_{12} between their wave vectors $\mathbf{Q}_1$ and $\mathbf{Q}_2$. Three fundamental types of helical domain walls have been reported recently in magnetic force microscopy imaging of B20 FeGe (*17*). Where $\theta_{12} \lesssim 85°$, "type I" walls are observed, which are smooth and free of disclination defects or phase mismatch. We found that for the parameters relevant for our MnGe films, the type I domain walls are energetically preferred.

Our micromagnetic modeling shows a distortion of the helices near the domain wall (Fig. 2, F and G). There are two characteristic surface projections depending on whether the $\mathbf{Q}_{1,2}$ vectors are oriented toward or away from the intersection domain wall plane. For **Q**s oriented toward the wall, the intersection plane is characterized by series of sharp, nested vertices along the domain wall (Fig. 2F). In contrast, for **Q**s oriented away from the wall, the domain wall is characterized by a nesting of more gradual, curved helices (Fig. 2G). In both cases, the surface projections $\mathbf{q}_1$, $\mathbf{q}_2$ make an in-plane angle $\phi_{12} = 120°$ independent of θ_{12}. The difference between these projections reflects rounding of the helical stripes in proximity to the domain wall and the surface.

In good agreement with our modeling, both projections of type I domain walls are observed experimentally (Fig. 2E, dashed boxes). The domain wall in the left box shows the nested, sharp vertex-like structure expected from Fig. 2F. By considering the 3D nature of $\mathbf{Q}_i$, we can extract the angle θ_{12} geometrically using

$$\cos\theta_{12} = \frac{Q_1 \cdot Q_2}{|Q_1||Q_2|} = \sin\theta_1 \sin\theta_2 \cos\phi_{12} + \cos\theta_1 \cos\theta_2 \quad (1)$$

where $\theta_1 = 26°$, $\theta_2 = 19°$ are the polar angles calculated in each domain from the period of the stripes, and $\phi_{12} = 113°$ is estimated as the angle between the stripe patterns on either side of the domain wall. (The simplest model that ignores surface effects predicts a 120° angle, as noted above.) This then gives an angle $\theta_{12} = 37°$ between $\mathbf{Q}_1$ and $\mathbf{Q}_2$ in this region, which is within the established regime for a type I domain wall (*17*). The right box in Fig. 2E shows the other surface projection of a type I domain wall, characterized by a nesting of rounded helical stripes, and can be analyzed in a similar way to give $\theta_{12} = 30°$, also within the type I regime.

More complex magnetic textures can be found at the intersections of domain walls. Our modeling shows that the intersection of two domain walls must necessarily involve at least one wall that is of type II or type III, which are energetically unfavorable and not observed experimentally (fig. S6). We found, however, that three type I domain walls can meet along an axis perpendicular to the surface and can lead to two distinct spin textures depending on the orientations of the $\mathbf{Q}_i$s. The spin texture in Fig. 3A results when all three **Q**s are oriented toward or away from the intersection axis, and exhibits a core region that is wrapped with closed helical loops. These textures closely resemble topological defects known as "target" states or 2π-disclination defects (*26*, *27*). The second "π" texture results from the arrangement of $\mathbf{Q}_i$ as shown in Fig. 3B. Both of these textures have nonzero topological charge density, concentrated in the vicinity of the domain walls, which

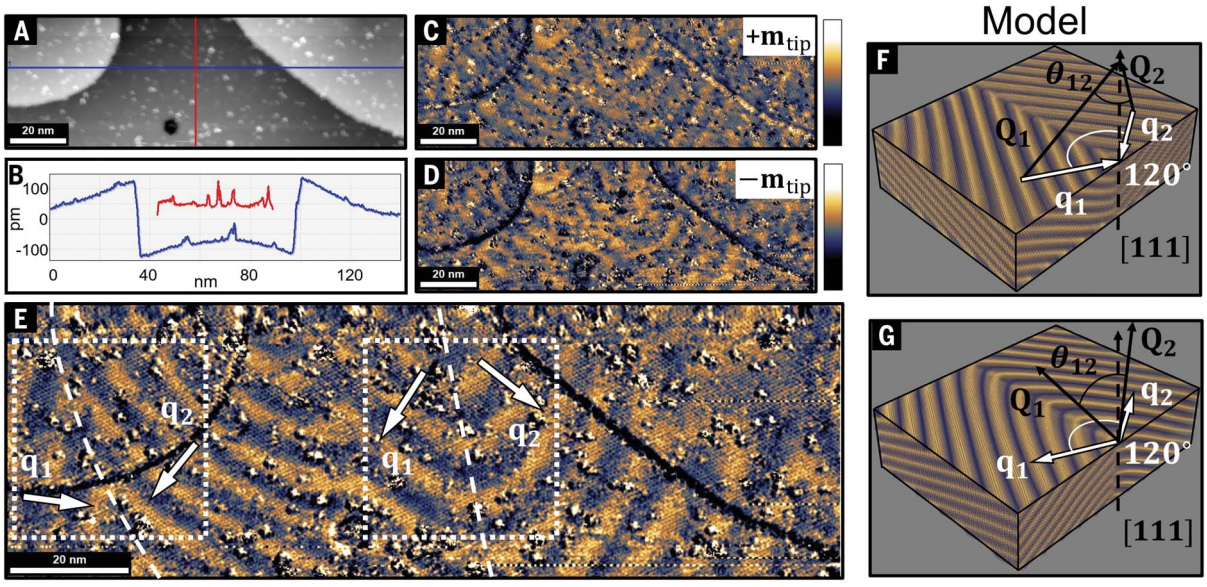

Fig. 2. Spectroscopic imaging of helical domains in a bowed region of the surface. (**A**) Topographic image of a bowed region of the surface containing three atomic terraces (0.17 V, 1.0 nA, T = 5 K). (**B**) Line profiles taken along the blue and red lines in (A). (**C** and **D**) Subsequent dI/dV images of the same region as in (A) (0.17 V, 1.0 nA). The contrast of the helical texture is subtly visible and inverts upon reversal of the tip magnetization vector $\mathbf{m}_{tip}$. (**E**) Difference image [(C) − (D)] showing a variety of helical textures. Two type I domain walls are boxed and indicated by the dashed lines. (**F**) Micromagnetic model of a domain wall where $\mathbf{Q}_1$ and $\mathbf{Q}_2$ are separated by an angle θ_{12} and point toward the intersection plane. The surface projections ($\mathbf{q}_1$, $\mathbf{q}_2$) intersect at a domain wall showing a nesting of sharp vertices. (**G**) Micromagnetic model of a domain wall where $\mathbf{Q}_1$ and $\mathbf{Q}_2$ point away from the intersection plane, resulting in a nesting of more rounded helices.

Fig. 3. Modeling and observation of target and π textures. (**A**) Micromagnetic model of the target spin texture, with arrows indicating surface **q**s pointing away from the intersection axis. This results in rounded triangular rings wrapping a central core. (**B**) Model of the π texture, where two **q** vectors point inward toward each other and the third points away, resulting in two rounded domain walls meeting a sharp domain wall. (**C**) SP-STM image of the target texture (−0.31 V, 0.22 nA). (**D**) SP-STM image of a π texture (−0.31 V, 0.20 nA). The SP-STM images in (C) and (D) are shown without additional processing. (**E**) Three-dimensional view of the area hosting the target texture, showing curvature of the surface. Topographic information is shown along the z axis and the color scale is a dI/dV overlay from the image shown in (C). (**F**) Line profiles taken along the x (blue) and y (red) directions in (E) to show in more detail the curvature of the surface in this area.

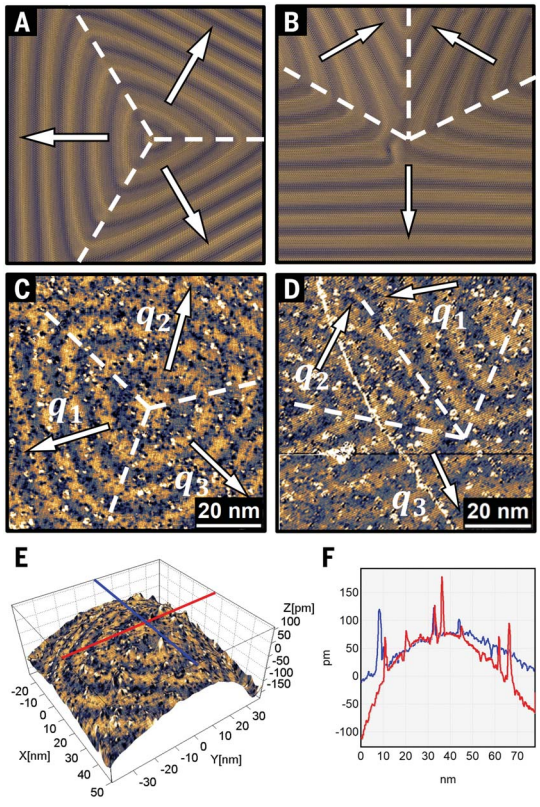

oscillates in sign as one moves outward from the core of the texture (fig. S9). In the absence of a well-defined boundary, however, neither the target nor the π texture have a quantized topological charge. Our modeling also shows that the core of the target texture consists of a string of alternating hedgehogs and anti-hedgehogs that is oriented perpendicular to the surface (fig. S10).

Experimentally, we found both the target and π textures in a region of the film where there was also nanoscale curvature. Figure 3C shows the conjunction of three type I walls to form the target texture, with closed helical loops wrapping around a central ~10-nm core. The isometric topographic image (Fig. 3E) and topographic linecuts (Fig. 3F) of this area indicate that the core is localized to the region of convex curvature to within a few nanometers in both the horizontal and vertical directions, although there was some variation in this proximity among the other target textures observed (fig. S14). Figure 3D shows the π texture in an adjacent region spanning two terraces separated by an atomic step across the middle. The local curvature in this region is slightly concave and connects adjoining regions with target textures and convex curvature (fig. S14).

Applications of magnetic skyrmions rely on the ability to manipulate these spin textures, which has been demonstrated with a variety of stimuli (*28*–*31*), including STM pulsing (*30*) and pressure (*31*). We found that the target texture can be similarly manipulated by local current/voltage pulses. Figure 4, A to D, shows a sequence of SP-STM images where current/voltage pulses were applied to the core region using the STM tip. The initial state of the target texture in Fig. 4A displayed a bright core and several surrounding closed loops. After imaging, the STM tip was positioned over the core and a short (0.5 s) current/voltage

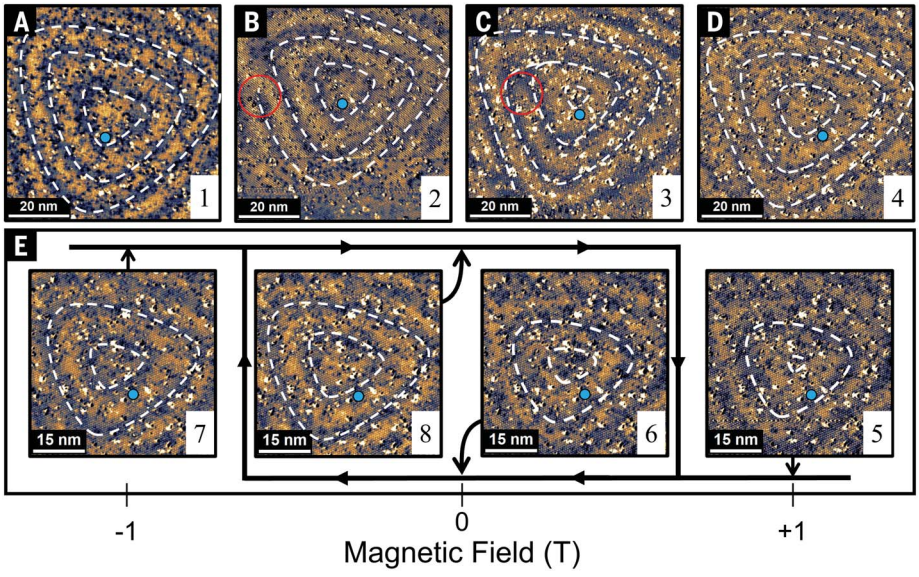

Fig. 4. STM tip and magnetic field manipulation of a target texture. (**A** to **D**) SP-STM images of the target spin texture in different configurations. Between each image, current/voltage pulses were applied with the STM tip (~2.0 V, 0.5 s, $I \lesssim 1\ \mu$A due to 300-pm approach). White dashed lines are guides to the eye showing wrapping around the core region. The red circle in (B) and (C) indicates a disclination defect that is generated, moved, and then annihilated. The blue dot represents the same atomically registered fixed point in the images, showing motion of the core. (**E**) SP-STM images showing the magnetic field dependence of the texture. Image 5, taken after image 4 with an out-of-plane magnetic field of +1 T, shows reversed contrast. Subsequent imaging (images 6 to 8) was performed in the indicated loop, with a clear hysteresis effect evident upon comparison of images 6 and 8. All images were taken under conditions of −0.3 V, 0.2 nA, and T = 5 K and are shown without any additional processing.

pulse was applied. A new disclination defect (branch point) appeared in the subsequent SP-STM image (Fig. 4B, red circle), which represents a discrete change in the topological charge density within this region. The core center also shifted by ~5 nm with respect to the fixed background of atomic defects. Subsequent pulsing shifted the disclination defect closer to the core, which itself changed contrast and size (Fig. 4C). A final cycle of pulsing annihilated the disclination defect and further shifted the core (Fig. 4D). Although this series of images was taken with different atomic tip terminations (and thus possibly different magnetic contrast), the topology of the final state was identical to the starting state (Fig. 4A). This indicates that the target texture had been reversibly manipulated through a landscape of metastable topological states.

We also observed hysteretic behavior of the target texture with applied out-of-plane magnetic field, as shown in Fig. 4E. After acquiring the SP-STM image at zero field (image 4 in Fig. 4D), the magnetic field was ramped up to +1 T. As shown in SP-STM image 5 in Fig. 4E, the core region is reduced in size and shows faintly dark contrast (dashed lines). Ramping the field back down to 0 T (image 6) shows an expansion of the wrapping and increased dark contrast of the core region. The core region flips back to bright contrast and shrinks when the field is ramped to −1 T (image 7), and then expands again when the field is ramped back down to 0 T (image 8). Comparing images 4 and 6 reveals a clear hysteresis effect, and the identical magnetic contrast in images 4 and 8 indicate that this effect is reversible. Consistent with previous SP-STM studies using bulk Cr tips (*30*), this hysteretic behavior cannot be explained as a field-dependent polarization of the tip. In fig. S17 we show SP-STM simulations indicating that if the tip polarization vector were changing with applied field, there would be changes in stripe contrast and/or anisotropy, which are not observed in Fig. 4E. Instead, our micromagnetic modeling explains the contrast reversal as arising from a net magnetic moment associated with the finite-volume texture, which aligns with the applied magnetic field. A π phase shift is induced when the magnetic field switches direction, leading to a reversal of contrast in the SP-STM images (fig. S10).

The topological spin textures observed in our thin films are distinct from those in bulk samples, which raises questions concerning the interplay of bulk and surface magnetism (*32*). How, or whether, the textures we observed extend into the bulk of the films can be further explored by comparing bulk measurements of topological Hall effect with magnetic imaging techniques such as (surface-sensitive) SP-STM and (volumetric) Lorentz transmission electron microscopy. Although additional study is needed to establish quantitative correlation, the association of these textures with local strain may reflect an interplay of magnetostriction effects, which have been studied in B20 materials (*33*–*35*), and further advances strain as an additional tuning parameter in thin-film devices for future memory and logic applications (*12*, *31*, *36*).

REFERENCES AND NOTES

1. A. Fert, N. Reyren, V. Cros, *Nat. Rev. Mater.* **2**, 17031 (2017).
2. A. Soumyanarayanan, N. Reyren, A. Fert, C. Panagopoulos, *Nature* **539**, 509–517 (2016).
3. R. Wiesendanger, *Nat. Rev. Mater.* **1**, 16044 (2016).
4. C. H. Back *et al.*, *J. Phys. D* **53**, 363001 (2020).
5. K. M. Song *et al.*, *Nat. Electron.* **3**, 148–155 (2020).
6. S. S. P. Parkin, M. Hayashi, L. Thomas, *Science* **320**, 190–194 (2008).
7. R. Tomasello *et al.*, *Sci. Rep.* **4**, 6784 (2014).
8. A. Fert, V. Cros, J. Sampaio, *Nat. Nanotechnol.* **8**, 152–156 (2013).
9. S. Mühlbauer *et al.*, *Science* **323**, 915–919 (2009).
10. X. Z. Yu *et al.*, *Nat. Mater.* **10**, 106–109 (2011).
11. N. Kanazawa *et al.*, *Phys. Rev. B* **86**, 134425 (2012).
12. T. Tanigaki *et al.*, *Nano Lett.* **15**, 5438–5442 (2015).
13. M. Bornemann *et al.*, *J. Phys. Condens. Matter* **31**, 485801 (2019).
14. T. T. J. Mutter, A. O. Leonov, K. Inoue, *Phys. Rev. B* **100**, 060407 (2019).
15. Y. Fujishiro, N. Kanazawa, Y. Tokura, *Appl. Phys. Lett.* **116**, 090501 (2020).
16. M. Deutsch *et al.*, *Phys. Rev. B* **90**, 144401 (2014).
17. P. Schoenherr *et al.*, *Nat. Phys.* **14**, 465–468 (2018).
18. See supplementary materials.
19. J. P. Corbett *et al.*, *ACS Appl. Mater. Interfaces* **12**, 9896–9901 (2020).
20. S. V. Grigoriev *et al.*, *Phys. Rev. Lett.* **110**, 207201 (2013).
21. M. Trabel *et al.*, *J. Appl. Phys.* **121**, 245310 (2017).
22. D. Morikawa *et al.*, *Phys. Rev. Mater.* **4**, 014407 (2020).
23. N. Kanazawa *et al.*, *Phys. Rev. B* **96**, 220414 (2017).
24. F. Li, T. Nattermann, V. L. Pokrovsky, *Phys. Rev. Lett.* **108**, 107203 (2012).
25. T. Nattermann, V. L. Pokrovsky, *J. Exp. Theor. Phys.* **127**, 922–932 (2018).
26. F. Zheng *et al.*, *Phys. Rev. Lett.* **119**, 197205 (2017).
27. D. Cortés-Ortuño *et al.*, *Phys. Rev. B* **99**, 214408 (2019).
28. W. Jiang *et al.*, *Science* **349**, 283–286 (2015).
29. N. Ogawa, S. Seki, Y. Tokura, *Sci. Rep.* **5**, 9552 (2015).
30. N. Romming *et al.*, *Science* **341**, 636–639 (2013).
31. Y. Nii *et al.*, *Nat. Commun.* **6**, 8539 (2015).
32. Y. Fujishiro *et al.*, *Nat. Commun.* **12**, 317 (2021).
33. E. Franus-Muir, M. L. Plumer, E. Fawcett, *J. Phys. C* **17**, 1107–1114 (1984).
34. A. E. Petrova, S. M. Stishov, *Phys. Rev. B* **94**, 020410 (2016).
35. Y. Hu, B. Wang, *New J. Phys.* **19**, 123002 (2017).
36. Y. Fujishiro *et al.*, *Nat. Commun.* **10**, 1059 (2019).
37. MnGe Data repository; https://doi.org/10.5281/zenodo.4013735.

ACKNOWLEDGMENTS

We thank S. Mueller for helpful discussions on the data analysis. **Funding:** Primary support was provided by DARPA grant D18AP00008. Partial support was provided by US Department of Energy grant DE-SC0016379 for SP-STM technique development. J.G.S. and N.T. thank DGAPA-UNAM projects IN101019 and IA100920 and CONACyT grant A1-S9070 of the Call of Proposals for Basic Scientific Research 2017–2018 for partial financial support. Calculations were performed in the DGCTIC-UNAM Supercomputing Center, project LANCAD-UNAMDGTIC-368. **Author contributions:** J.R. and J.P.C. performed SP-STM experiments and analyzed data; T.L.,T.Z., S.C., and A.S.A. grew the thin films and characterized the structural and magnetic properties; P.-K.W. and M.R. performed theoretical modeling; N.T. and J.G.-S. performed density functional theory calculations for the surface structural study; and R.K.K., M.R., and J.A.G. helped in writing the manuscript and analyzing the results. **Competing interests:** The authors declare no competing interests. **Data and materials availability:** See (*37*).

SUPPLEMENTARY MATERIALS

science.org/doi/10.1126/science.abd9225
Materials and Methods
Supplementary Text
Figs. S1 to S19
References (*38*–*43*)
Movie S1

20 July 2020; accepted 19 October 2021
10.1126/science.abd9225

Atomic-scale visualization of topological spin textures in the chiral magnet MnGe

Jacob RepickyPo-Kuan WuTao LiuJoseph P. CorbettTiancong ZhuShuyu ChengAdam S. AhmedN. TakeuchiJ. Guerrero-SanchezMohit RanderiaRoland K. KawakamiJay A. Gupta

Science, 374 (6574), • DOI: 10.1126/science.abd9225

Peeking into magnetic textures

Topological spin textures hold promise as robust carriers of information and have been observed in bulk materials with a specific crystal structure. One of these materials, manganese germanide (MnGe), exhibits unusual textures in bulk form. Repicky *et al*. used spin-polarized scanning tunneling microscopy to study surface magnetism in thin films of MnGe. Achieving high spatial resolution, the researchers observed stripe-like features consistent with a helical state. In regions where the film was slightly curved due to strain, the intersection of domain walls led to characteristic closed patterns that could be manipulated with current/voltage pulses. —JS